Journal of Solid State Chemistry **142,** 220–227 (1999)
Article ID jssc.1998.8038, available online at http://www.idealibrary.com on IDEAL®

Raman Spectroscopy of Perovskite-Type $BaCe_xZr_{1-x}O_3$ ($0 \leq x \leq 1$)

I. Charrier-Cougoulic, T. Pagnier,[1] and G. Lucazeau

Laboratoire d'Electrochimie et de Physicochimie des Matériaux et Interfaces, INPG-CNRS, Enseeg 1130, rue de la Piscine, 38402 Saint-Martin-d'Hères Cedex, France

Received April 21, 1998; in revised form September 17, 1998; accepted September 17, 1998

Polycrystalline samples of $BaCe_xZr_{1-x}O_3$ were prepared by solid state reaction. X-ray diffraction measurements show that all compounds are single-phase and XRD patterns can be indexed on the basis of the ideal perovskite structure. However, Raman data show that $BaCe_xZr_{1-x}O_3$ exhibits slight x-dependent distortions from the ideal perovskite structure. Indeed the evolution of Raman spectra of $BaCe_xZr_{1-x}O_3$, as x decreases at room temperature or as temperature increases for a given x value, is similar to the evolution of Raman spectra of $BaCeO_3$ as temperature increases. These observations lead us to propose a phase diagram in the binary system $BaCeO_3$–$BaZrO_3$ based on the known structures of $BaCeO_3$ (*Pnma, Imma, R*$\bar{3}$*c*, and *Pm*3*m*).

1. INTRODUCTION

Among perovskite-type electrolytes, rare earth-doped $BaCeO_3$ exhibits a good proton conduction in atmospheres containing hydrogen and/or water vapor at elevated temperatures (1). However, this compound is not stable enough from chemical and mechanical points of view for electrochemical applications (2). $BaZrO_3$ has been found to be chemically more stable and to have better mechanical properties with respect to $BaCeO_3$ (2). Nevertheless proton conduction in doped zirconates is lower (2).

A recent study of the Yb-doped $SrCe_xZr_{1-x}O_3$ solid solution (3) showed an enhancement of the mechanical properties without loss of the electrical conductivity for $x = 0.75$. As rare earth-doped $BaCeO_3$ is the prototype for ceramic protonic conductors, it was interesting to study the effect of Zr substitution for Ce in this material.

In this paper, we present a structural study of seven compositions in the system $BaCe_xZr_{(1-x)}O_3$ ($x = 1$, 0.8, 0.6, 0.4, 0.2, 0.1, and 0) by X-ray diffraction and Raman spectroscopy: A complete solubility of $BaCeO_3$ and $BaZrO_3$ is found. As the two end members belong to different crystallographic space groups (orthorhombic *Pnma* for $BaCeO_3$ (4) and cubic *Pm*3*m* for $BaZrO_3$ (5)), this result is somewhat surprising. As a consequence, the structure of the mixed compounds evolves gradually from one structure to the other. This evolution is followed by Raman spectroscopy.

[1]To whom correspondence should be addressed.

2. EXPERIMENTAL SECTION

2.1. Sample Preparation

$BaCe_xZr_{1-x}O_3$ ($0 \leq x \leq 1$) samples were prepared by solid state reaction. High purity powders of $BaCO_3$ (Rhône-Poulenc), CeO_2 (Rhône-Poulenc), and ZrO_2 (Tosoh) in stoichiometric amounts were mixed for 15 h. The mixture was first calcined in air at 950°C for 15 h in order to prevent an irreversible expansion during sintering due to $BaCO_3$ decarbonatation. Powders were then ground in an agate mortar and pressed into pellets at an uniaxial pressure of 50 MPa followed by isostatic pressure at 250 MPa. Sintering was performed in air at 1500°C for 10 h. A wet chemical analysis showed that the Ce/Zr ratio was that expected for all samples. Electrical impedance measurements were performed in air up to 900°C and there was no indication of an electronic conduction: Ce and Zr are therefore assumed to be in a 4+ state.

2.2. X-Ray Diffraction Measurements

Routine X-ray diffraction measurements were carried out at room temperature using a Siemens $\theta/2\theta$ diffractometer with Cu$K\alpha_1$ radiation. Cell parameter refinements were performed with the software Unit Cell (6). Positions, areas, and half-widths at half maximum (HWHM) of X-ray diffraction peaks were determined by deconvolution of Gaussian-shaped peaks with Peakfit software (JANDEL).

2.3. Raman Spectroscopy

The exciting line of an argon ion laser (wavelength of 514.53 nm) was focused on samples through an objective ($G = 50\times$) of a microscope and the scattered light was collected in a backscattering geometry. For all samples, Raman spectra were also collected at room temperature

0022-4596/99 $30.00

with the 488.00-nm line of the same laser. There was no difference in the Raman spectra with both wavelengths. A laser power of 20 mW, which corresponds to about 4 mW on sample surface, was used to avoid overheating. Raman spectra were obtained using a DILOR XY spectrometer with a CCD detector cooled with liquid nitrogen.

Samples were put in a LINKAM HFS 91 cooling–heating device placed underneath the microscope in 80% N_2–20% O_2 dry atmosphere. Their Raman spectra were recorded between room temperature and 873 K. Band position and width were determined with the Peakfit software (JANDEL) using Lorentzian-shaped functions.

3. RESULTS

3.1. X-ray Diffraction

XRD patterns of $BaCe_xZr_{1-x}O_3$ ($0 \leq x \leq 1$) samples are shown in Fig. 1. The room temperature structure of $BaCeO_3$ is orthorhombic (*Pnma*). It corresponds to a small distortion of the cubic structure, which was demonstrated using neutron diffraction by Jacobson (4). $BaCeO_3$ evolves slowly toward cubic ideal perovskite structure upon heating: phase transitions occur at 560 K (orthorhombic, *Imma*), at 670 K (rhombohedral, $R\bar{3}c$), and at 1170 K (cubic, *Pm*3*m*) (7, 8). This cannot be easily observed using X-ray diffraction measurements because of the very small distortion of the ideal cubic structure. On the other hand, $BaZrO_3$ is cubic at room temperature (5, 9).

All XRD patterns were analyzed in the approximation of a cubic unit cell. The averaged *a* parameter is shown as a function of *x* in Fig. 2. The relationship between *a* and *x* is roughly linear. The *a* value for $BaZrO_3$ (4.1918 Å) is consistent with the published one (5) and that for $BaCeO_3$ (4.3867 Å) is similar to the average value obtained from neutron diffraction (7).

A closer examination of the line shapes shows that their full width at half maximum (FWHM) is not constant (Fig. 3). The smallest FWHMs are obtained for $BaZrO_3$. Peaks are slightly broadened for $BaCeO_3$: this can be attributed to its orthorhombic distortion. For all peaks, the FWHM presents a maximum between $x = 0.4$ and $x = 0.6$.

3.2. Raman Spectroscopy

Room temperature Raman spectra of $BaCe_xZr_{1-x}O_3$ ($0 \leq x \leq 1$) samples are shown in Fig. 4. For $x = 0$ and $x = 0.1$, Raman spectra show a very low intensity (notice the multiplicative factors of 18 and 33 in Fig. 4) and only broad bands are visible. This result is expected for materials belonging to the *Pm*3*m* space group. In principle, there should be no Raman spectrum, as it has been pointed out (9). The most probable explanation for the spectra observed here is that they are of second order. The other spectra show narrow bands which are close to those of $BaCeO_3$ and broad weak bands which may also be of second order. The $BaCeO_3$ Raman spectrum is similar to that already published (10). At room temperature, 9 of the expected 24 Raman-active modes in the orthorhombic structure are easily observed. All bands ranging from 80 to 400 cm^{-1} are generated by first-order modes, whereas higher-

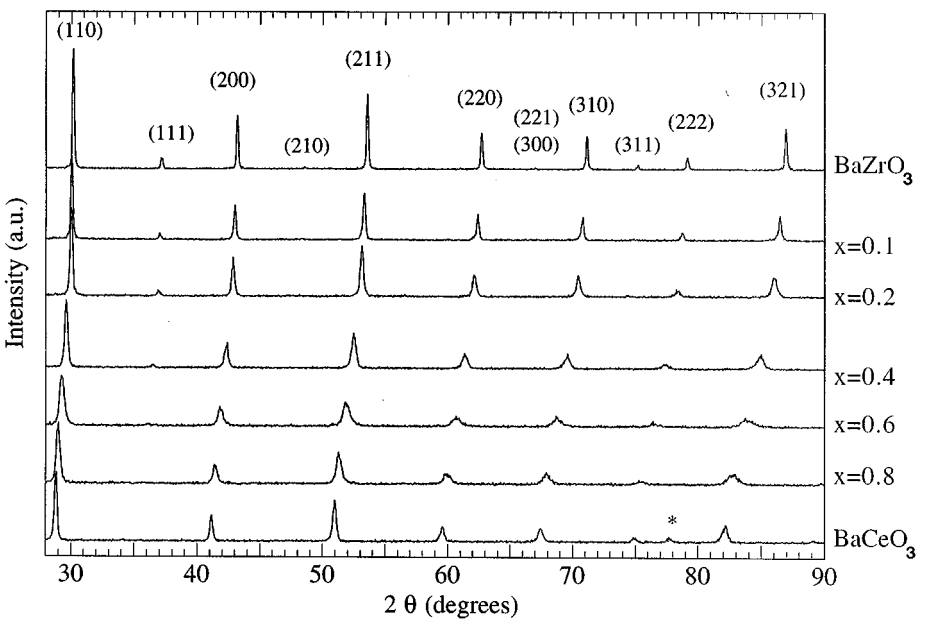

FIG. 1. XRD patterns of $BaCe_xZr_{1-x}O_3$ ($0 \leq x \leq 1$) samples obtained with Cu$K\alpha_1$ radiation (Miller indices correspond to a primitive cubic system. *Peak due to sample holder.

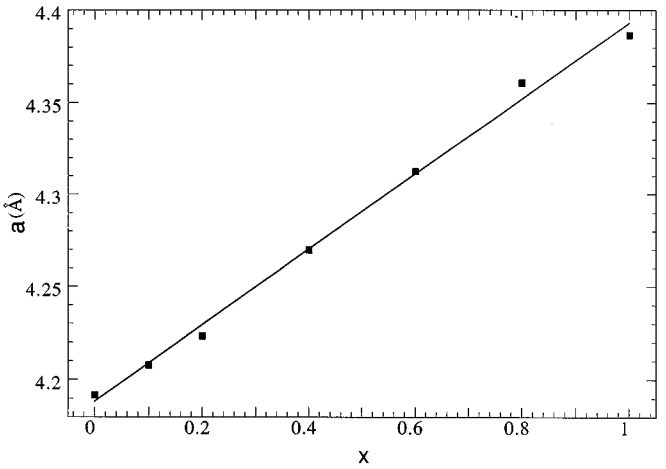

FIG. 2. Cell parameter a in $BaCe_xZr_{1-x}O_3$ $(0 \leq x \leq 1)$ samples (pseudocubic cell).

wavenumber Raman bands are probably due to multiphonon or electronic Raman processes (10, 11).

For $x \geq 0.2$, one may distinguish between two groups of bands with different behaviors. Below 150 cm^{-1}, three bands (bands 1 to 3 in Fig. 4) appear in the $BaCeO_3$ spectrum. Two bands remain for $x = 0.8$ and $x = 0.6$ and only one for $x = 0.4$ and $x = 0.2$. Notice also that the frequency of these bands depends slightly on composition (Fig. 5a): band 1″ of Fig. 4 shifts toward lower wavenumbers by less than 1 cm^{-1} for x varying from 0.4 to 0.2. The other group is composed of the bands labeled 4 to 6 in Fig. 4. Band 4 is present in all spectra with almost the same intensity. Band 5 is present from $x = 1$ to $x = 0.4$ and band 6 from $x = 0.8$ to $x = 0.2$. Besides, an intensity transfer occurs between these two bands. All these bands display a strong frequency dependence upon composition (Fig. 5b).

Raman spectra were also collected at various temperatures. For $BaCeO_3$, spectra were similar to those already published (10). Two examples are shown in Figs. 6 ($x = 0.8$) and Fig. 7 ($x = 0.4$). For $x = 0.8$, the major changes that are observed are the broadening of all peaks. Notice also that the two low wavenumber bands (1′ and 2′ of Fig. 4) are still visible at 373 K, but there is only one band in this region at temperatures higher than 573 K. For $x = 0.4$, all the narrow bands have disappeared at 773 K, suggesting that the structure is cubic at this temperature.

4. DISCUSSION

4.1. Mutual Solubility of $BaCeO_3$ and $BaZrO_3$

Both XRD patterns and Raman spectra indicate that $BaCeO_3$ and $BaZrO_3$ are mutually soluble in all proportions. The presence of well-developed crystallites of either end member would have been detected in X-ray diffraction experiments. $BaCeO_3$ has a strong first order Raman spectrum and its presence should have been observed in the Raman spectra of the mixed compounds, even for very small crystallites, of the order of 10 nm. On the contrary, the linear relation between the pseudocubic cell parameter and

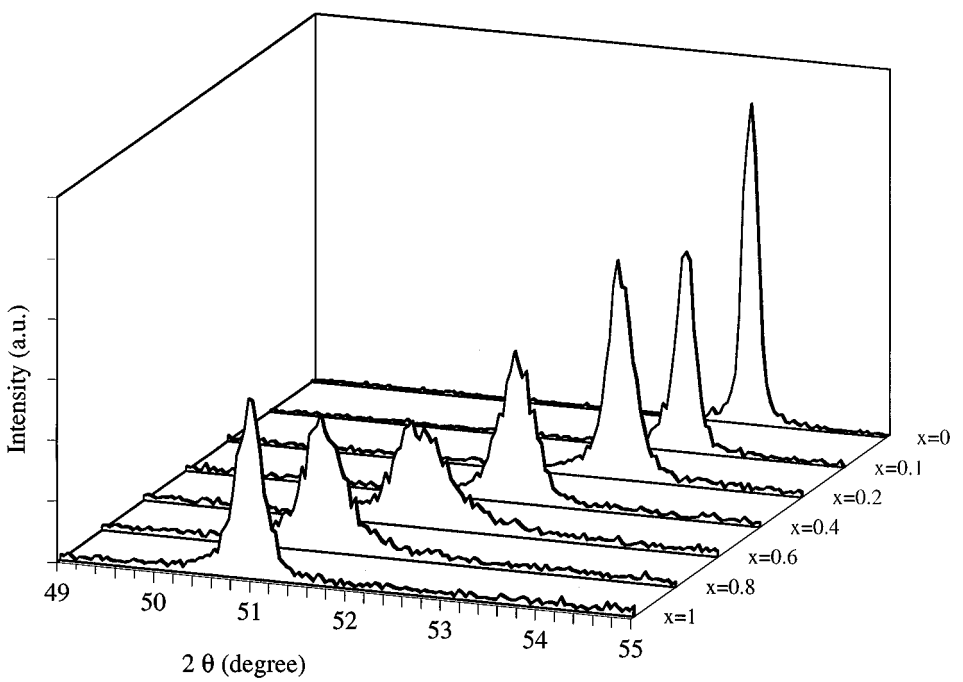

FIG. 3. Emphasis on X-ray diffraction peak in $BaCe_xZr_{1-x}O_3$ as a function of x corresponding to (211) Miller indices in the cubic structure.

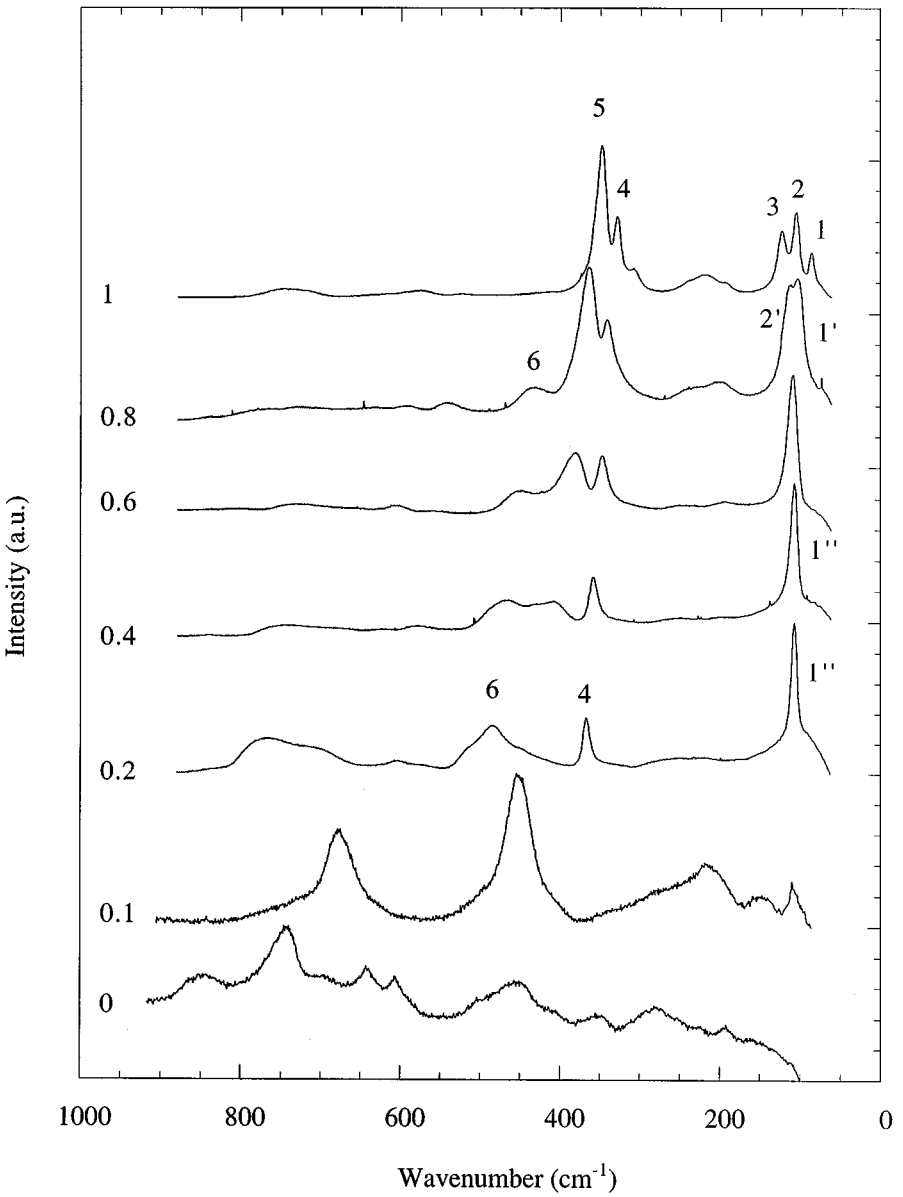

FIG. 4. Raman spectra of $BaCe_xZr_{1-x}O_3$ samples at room temperature. x values are indicated on the left of each spectrum. Spectra for $x = 0$ and $x = 0.1$ were multiplied by a factor of 18 and 33 before drawing.

x, the shift in wavenumber of Raman bands 4 to 6 are indications of a strong mixing effect and therefore of mutual solubility. Complete solubility was also proposed in the case of $SrCe_xZr_{1-x}O_3$ (3). Line broadening in XRD patterns suggests that the mixed material structure is slightly more distorted than that of $BaCeO_3$ and that unresolved superstructure is responsible for this broadening.

As a first approximation, one may describe the mixed materials as follows: the structure is that of a slightly distorted perovskite ($x \geq 0.2$), to allow first-order Raman spectra. For Ba and O atoms, the translational invariance is maintained, while Ce and Zr atoms are randomly (or almost randomly) distributed over the B sites of the perovskite structure. This model is often found (for an old, but still pertinent review, see (12)) in mixtures of materials having similar (but not necessarily identical) structures.

For the samples with $x = 0$ and $x = 0.1$, Raman spectra indicate that they are cubic. The strong difference between room temperature Raman spectra of both samples is surprising. Also surprising is the relative simplicity of the Raman spectrum of the $BaCe_{0.1}Zr_{0.9}O_3$ sample. We have

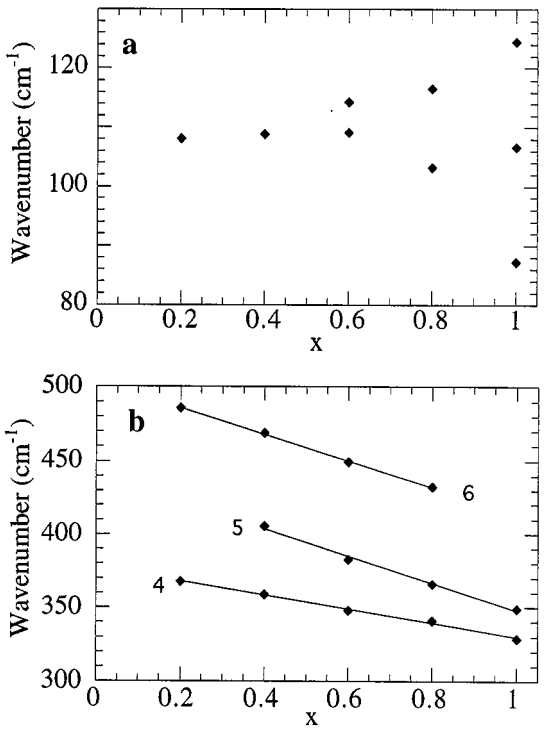

FIG. 5. Changes in the band position for bands 1 to 3 (a) and 4 to 6 (b) as a function of x.

no explanation for these observations. In the following, we will discuss only the results obtained for $x \geq 0.2$.

4.2. Assignment of the Narrow Raman Bands

Band attribution has been made by Genet *et al.* (10) in the case of $BaCeO_3$. They also deduced the potential energy distribution (PED) from a normal mode analysis. Bands below 150 cm^{-1} (bands 1 to 3 in Fig. 4) are mostly due to Ba–O stretching and O–Ba–O bending force constants. The band at 330 cm^{-1} (band 4) involves Ba–O stretching and O–Ce–O bending with similar PED coefficients. The band at 350 cm^{-1} (band 5) is almost exclusively correlated to Ce–O stretching force constant. With the same attributions in the mixed compositions, one may expect a sensitivity to Ce–Zr substitution varying from low (bands below 150 cm^{-1}) to medium (band 4) and to high (band 5); that is the observed behavior. It is interesting to notice that bands 5 and 6, for which a transference of intensity seems to occur, may be related to Ce–O and Zr–O stretching. The extrapolation of band 6 position at $x = 0$ gives a value of 504 cm^{-1} for pure $BaZrO_3$ ($x = 0$). This value is close to that obtained for the Zr–O stretching band in cubic $BaZrO_3$ (13) deduced from infrared reflectivity measurements (505 cm^{-1}). All these results indicate that the band attribution for $BaCeO_3$ is still valid in the mixed compounds.

4.3. High Wavenumber Bands: Indicators of Force Constant Changes

Following the conclusion of the previous section, these bands (bands 4–6 in Fig. 4) predominantly involve Ce–O and Zr–O force constants (stretching and bending). In addition, Ce and Zr atoms are located at inversion centers and do not move in the g modes. Raman spectra of solid solutions obtained by replacing one kind of atom for another one have been extensively studied. Linear chain models have been used (12) to understand the major effects of this substitution. At the microscopic scale, the perovskite structure can be described by a tridimensional network of MO_6 octahedra. In $BaCeO_3$, these octahedra are all CeO_6. When one Zr atom is substituted for one Ce atom, the ZrO_6 octahedron is submitted to forced oscillations by its neighbors and vibrates in phase with them. As the amount of Zr increases, this trend may disappear. Coupling between ZrO_6 and CeO_6 first neighbors and then between ZrO_6 and ZrO_6 first neighbors becomes more and more important. If the masses of the two atoms and the force constants involved are not too different, a one mode behavior can appear (e.g., $Sr_xBa_{1-x}F_2$ (14)). The band frequency shifts progressively from its value at one end member to that at the other end member. On the other hand, if masses or force constants are too different, the situation becomes highly complex. Linear chain simulations indicate that many modes can appear. In this situation, a two mode behavior is expected. The two-mode behavior ($Si_{1-x}Ge_x$ (15)) is characterized by the simultaneous presence of the two end-member bands in the mixed crystal, sometimes associated with "gap" or "local" modes ranging between them. In $Si_{1-x}Ge_x$, these bands have been attributed to Si–Si, Si–Ge and Ge–Ge modes. Both behaviors can appear simultaneously in the same material, depending on the band investigated (12). In the case of $BaCe_xZr_{1-x}O_3$, band 4 displays a one-mode behavior, and bands 5 and 6 a two mode behavior.

The evolution of these bands upon heating is customary: in all cases, a broadening and a decrease in amplitude is observed.

4.4. Low Wavenumber Bands: Indicator for Structural Changes

It is clear that the discussion in Section 4.3 cannot apply to the low wavenumber part of the Raman spectra. Raman band disappearance is associated with a structural change toward a more symmetric structure connected to a change in the selection rules. Surprisingly, the changes depicted in Fig. 5a fully mimic those observed in $BaCeO_3$ as a function of temperature (8, 16). Because of the influence of crystal symmetry on the appearance of Raman bands, this result strongly suggests that the structural changes in $BaCe_xZr_{1-x}O_3$ as a function of Zr content are the same as

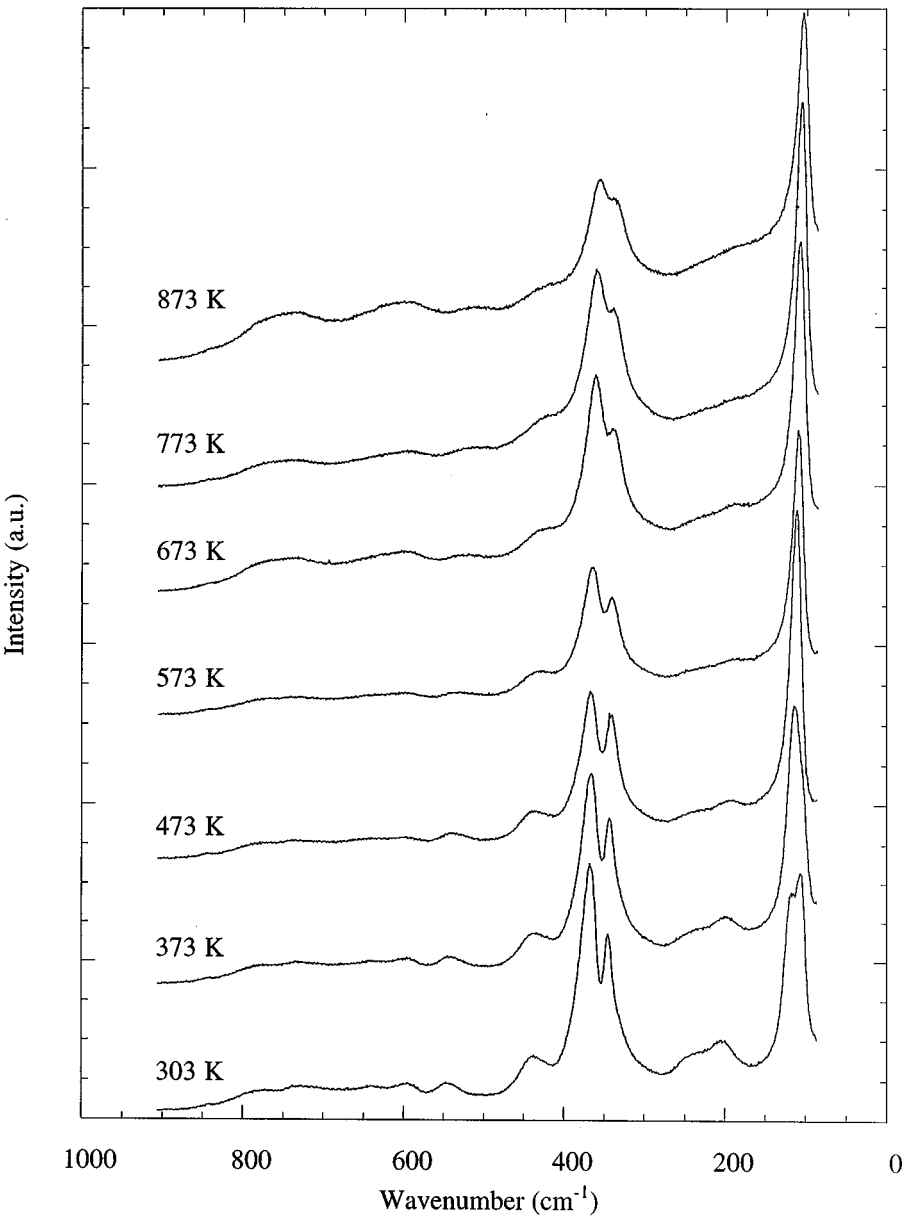

FIG. 6. Raman spectra of $BaCe_{0.8}Zr_{0.2}O_3$ at various temperatures in dry air.

those observed in $BaCeO_3$ as a function of temperature. To explain this, two remarks can be made. At first, from a structural point of view, both the starting point (orthorhombic $BaCeO_3$ at room temperature) and the end points (cubic $BaZrO_3$ at room temperature, cubic $BaCeO_3$ at high temperature) are the same. Second, $BaCeO_3$ distortion at room temperature is due to the large ionic radius of Ce^{4+}, from which a Goldschmidt tolerance factor far lower than unity can be computed. Because of the thermal expansion, there is more room for the CeO_6 octahedra when heating $BaCeO_3$ and the tolerance factor progressively increases up to the value of 1, which is that of a cubic structure. Upon substituting Zr for Ce, the size of the MO_6 (M = Ce, Zr) octahedra decreases, but the tolerance factor increases up to unity in $BaZrO_3$ and $BaCe_{0.1}Zr_{0.9}O_3$. Finally, one may observe that these low wavenumber bands are mostly dependent on Ba–O and O–Ba–O force constants. The progressive decrease of the number of bands in this region is the indication that Ba and O atoms progressively shift toward more symmetric positions. We therefore propose that the number of observed bands in the 80–150 cm^{-1} region can be used as an indicator of the structure of the solid solution. When

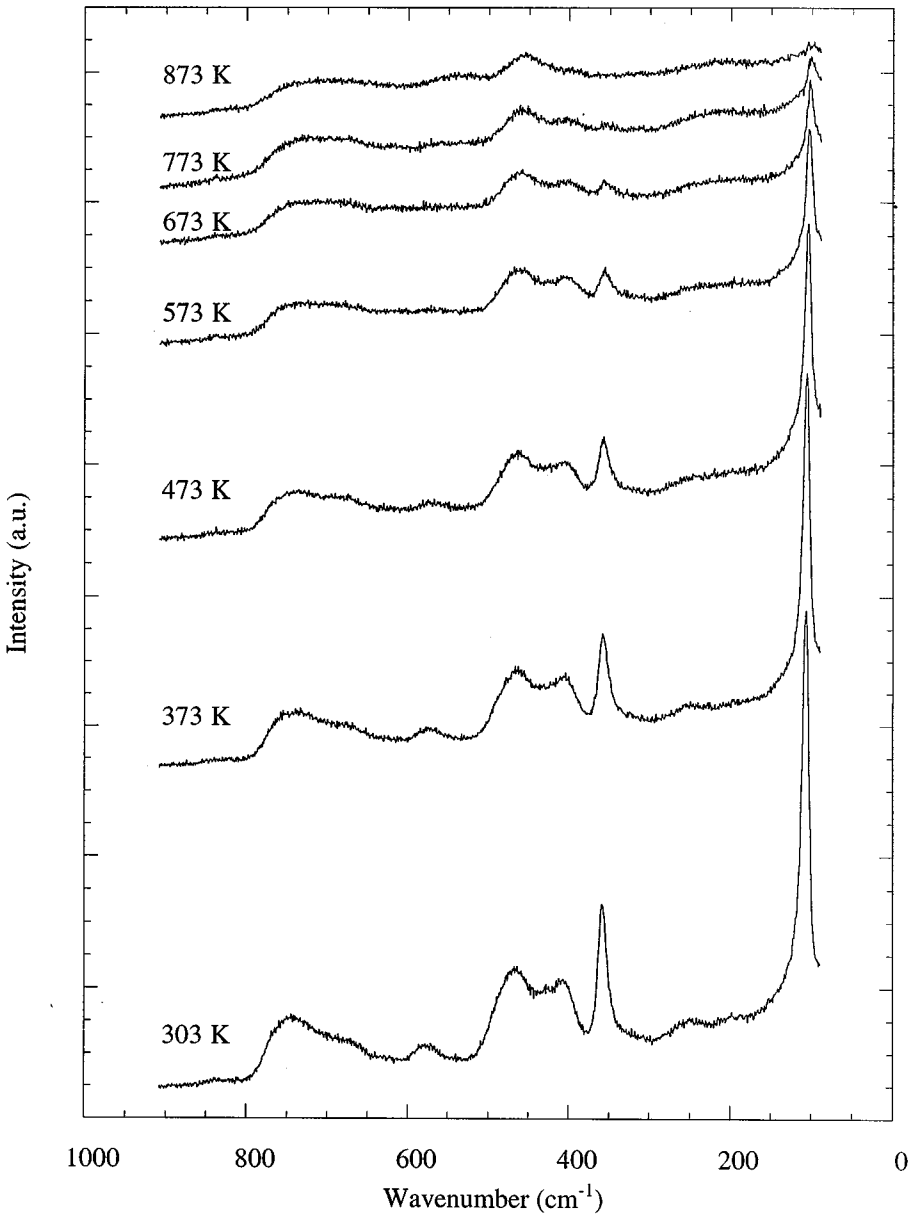

FIG. 7. Raman spectra of $BaCe_{0.4}Zr_{0.6}O_3$ at various temperatures in dry air.

three bands are present, the space group is *Pnma*, as for $BaCeO_3$. Two bands are characteristic of the *Imma* space group, one band of $R\bar{3}c$ and no band of the ideal cubic structure. Following this conclusion, the room temperature structure of the solid solutions is cubic for $x \leq 0.1$, rhombohedral for $x \leq 0.2$ and $x = 0.4$, orthorhombic (*Imma*) for $x = 0.6$ and $x = 0.8$ and orthorhombic *Pnma* for $x = 1$.

The changes in the Raman spectra as a function of temperature give additional evidence for our interpretation. The general tendency of distorted perovskites is to become cubic on heating. Figure 6 shows that two bands are present near $100\,cm^{-1}$ at room temperature and that only one band is visible for temperatures higher than 473 K. A similar observation can be made for $x = 0.6$ (data not shown). For $x = 0.4$ and $x = 0.2$, which display only one band at room temperature, the $R\bar{3}c \rightarrow Pm3m$ transition occurs at about 700 K ($x = 0.4$) and 500 K ($x = 0.2$) and is indicated by the disappearance of all the narrow bands of the spectrum.

We therefore propose that the number of bands in the low wavenumber part of the Raman spectra can be used for

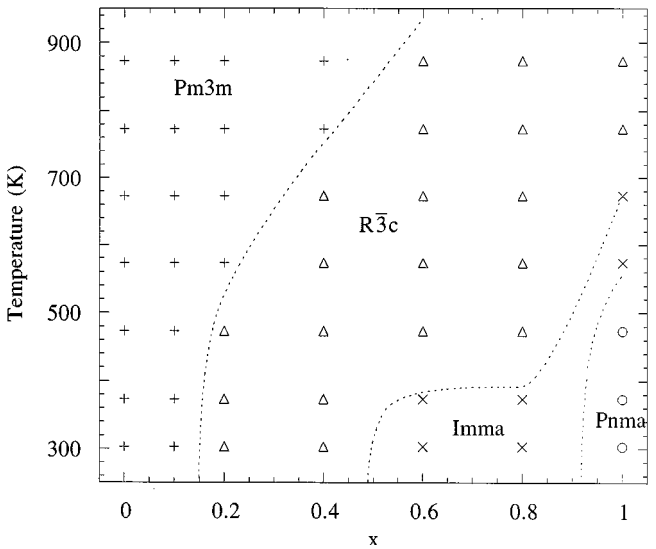

FIG. 8. Phase diagram of $BaCe_xZr_{1-x}O_3$ established in following the number of Raman lines near 100 cm^{-1} (+ , no line or *Pm3m*; △, 1 line or *R*$\bar{3}$*c*); ×, 2 lines or *Imma* and ○, 3 lines or *Pnma*).

drawing a phase diagram of the solid solutions. This was done in Fig. 8. From this figure, the major effect of Zr for Ce substitution is that it decreases the transition temperatures of $BaCeO_3$. This is not surprising, because this substitution decreases the size of the MO_6 octahedra and therefore decreases the driving force for the distortion.

We must point out that the phase diagram that we propose is not based on direct experimental evidence. Neutron diffraction studies of some of the samples are planned to confirm it.

5. CONCLUSION

Seven compositions in the $BaCe_xZr_{1-x}O_3$ system have been investigated by X-ray diffraction and Raman spectroscopy. All samples appear to be single-phase and a complete solubility exists between $BaCeO_3$ and $BaZrO_3$. For $x \leq 0.1$, the materials have the cubic structure. Their Raman spectra are most probably second order, but display interesting features that are not understood up to now. For $x \geq 0.2$, two groups of narrow bands show a different behavior when Zr for Ce substitution takes place. The high wavenumber bands, which are mostly due to force constants involving Ce and Zr atoms, display a shift in frequency reflects the substitution. The low wavenumber bands involve mostly Ba and O atoms. The number of bands in this region decreases when Zr content increases or when temperature rises. This is attributed to a progressive shift of Ba and O atoms toward more symmetric positions, which induces a change in the structure of the material. These transitions are very similar to those observed for $BaCeO_3$ upon heating and we propose a phase diagram based on these considerations.

REFERENCES

1. T. Scherban, W-K. Lee, and A. S. Nowick, *Solid State Ion.* **28–30,** 585 (1988).
2. H. Iwahara, T. Yajima, T. Hibino, K. Ozaki, and H. Suzuki, *Solid State Ion.* **61,** 65 (1993).
3. T. Matzke and M. Cappadonia, *Solid State Ion.* **86–88,** 659 (1996)
4. A. J. Jacobson, B. C. Torfield, and B. E. F. Fender, *Acta Crystallogr. B* **28,** 956 (1972).
5. Card 6-399, Powder Diffraction file, JCPDS International Center for Diffraction Data, 1995.
6. Unit Cell, TUB Holland and SAT Refden, Department of Earth Sciences, Cambridge CB2 3EQ, UK, 1995.
7. K. S. Knight, *Solid State Ion.* **74,** 109 (1994).
8. F. Genet, S. Loridant, C. Ritter, and G. Lucazeau, submitted for publication.
9. A. E. Pasto and R. A. Condrate, Sr., *in* "Advances in Raman Spectroscopy" (J. P. Mathieu, Ed.), Vol. 1. p 196. Heiden & Son, London, 1973.
10. F. Genet, S. Loridant, and G. Lucazeau, *J. Raman Spectrosc.* **28,** 255 (1997).
11. S. Loridant, L. Abello, and G. Lucazeau, *J. Raman Spectrosc.* **28,** 283 (1997).
12. A. S. Barker, Jr., and A. J. Sievers, *Rev. Mod. Phys.* **47** (Suppl. 2), S1 (1975).
13. C. H. Perry and D. J. McCarthy, *Phys. Rev.* **118,** A1537 (1965).
14. R. K. Chang, B. Lacina and P. S. Pershan, *Phys. Rev. Lett.* **17,** 755 (1966).
15. M. I. Alonso and K. Winer, *Phys. Rev. B* **39,** 10056 (1989).
16. T. Scherban, R. Villeneuve, L. Abello, and G. Lucazeau, *J. Raman Spectrosc.* **24,** 805 (1993).